Atomic-scale understanding of enhanced polarization of highly strained nanoscale columnar $PbTiO_3$

Y. Z. Dai,[1,2] L. Lu,[2] F. Zhang,[2] L. Jin,[3] Y. Jiang,[4] D. W. Wang,[2] Z. P. Li,[4,*] and C.-L. Jia[1,2,3,†]

[1]*State Key Laboratory for Mechanical Behavior of Materials, Xi'an Jiaotong University, Xi'an 710049, China*

[2]*School of Microelectronics & Key Lab of Micro-Nano Electronics and System Integration of Xi'an City, Xi'an Jiaotong University, Xi'an 710049, China*

[3]*Ernst Ruska-Centre for Microscopy and Spectroscopy with Electrons (ER-C), Forschungszentrum Jülich GmbH, 52425 Jülich, Germany*

[4]*School of Materials Science and Engineering, Beijing Advanced Innovation Center for Materials Genome Engineering, University of Science and Technology Beijing, Beijing 100083, China*

(Received 12 May 2021; revised 11 October 2021; accepted 1 November 2021; published 16 November 2021)

Spontaneous polarization in displacive ferroelectric oxides originates from the separation of positive charge centers from negative charge centers, which is induced by the off-center displacements of cations and anions in unit cells. For hugely strained ferroelectric oxides, understanding the correlation between the off-center displacements and the strain level is a prerequisite for understanding the polarization behavior. In the present work, the off-center displacements of atoms in nanometer columnar $PbTiO_3$ under a strong tensile strain of 13% along the ***c***-axis direction are quantified by quantitative high-resolution transmission electron microscopy. The measured off-center displacement Δ_{Ti-O} (0.052 nm) is about 60% larger than the value of unstrained bulk $PbTiO_3$. The experimental results are confirmed by first-principle calculations, leading to a polarization of 122 $\mu C/cm^2$, providing the basis for understanding the enhanced spontaneous polarization of highly strained displacive ferroelectric oxides.

DOI: 10.1103/PhysRevB.104.184111

I. INTRODUCTION

Strain engineering realized by deliberately selecting different substrates and controlling film thickness has been proven a powerful and accessible method to manipulate the properties of ferroelectric oxide thin films [1–3]. For instance, a biaxial compressive strain has been introduced to markedly enhance the ferroelectric transition temperature and the remnant polarization in $BaTiO_3$ [4], while the tensile strain was found to induce room-temperature ferroelectricity in $SrTiO_3$ [5]. Beyond this conventional approach for controlling the horizontal strain, vertical strain engineering via interfacial coupling between self-assembled components in the vertically aligned nanocomposite (VAN) system has been developed recently [1,6]. Microstructure and physical properties of the VANs were demonstrated to be related to the vertical strain state, which could be tuned by the selection of a suitable secondary phase and the control of the grain morphology, the column aspect ratio, and/or density distribution and so on [6–10].

$PbTiO_3$ (PTO) is a representative perovskite ferroelectric oxide with strong polarization-tetragonality coupling [11]. Thin films of PTO and PTO-based perovskite ferroelectric oxides epitaxially grown on diverse substrates have shown abundant ferroelectric phenomena and thus attracted tremendous research interests [12–21]. Recently, Zhang *et al.* implemented the concept of interphase strain to induce a large negative pressure (i.e., tensile strain) in PTO epitaxial composite thin films via PbO on the $SrTiO_3$ (STO) substrate [22]. That PTO film demonstrated a supertetragonality and a great enhancement of the remnant polarization. The experimental results stimulated research interest in fully understanding the underlying details of the structural phenomenon, in particular the nanometer-scale microstructure and the atom positions in the highly strained unit cell. For displacive ferroelectric oxides, polarization results from the formation of unit-cell dipoles that are directly related to the relative displacements of the cations from the oxygen anions in a unit cell. A particular interest of research is to understand how these ions behave under very large strain, whether the displacements of ions follow the polarization-tetragonality coupling, and how the experiment results compare to theoretical calculations.

In the present study, we report a systematic investigation of self-assembled VAN thin films with embedded nanometer PTO columnar grains surrounded by the PbO-type structural phase, prepared by pulsed laser deposition [23,24]. The atomic structure and the strained state of both the PTO columnar grains and the surrounding PbO-type structural phase are characterized by aberration-corrected (scanning) transmission electron microscopy [(S)TEM]. In particular, the negative spherical aberration (C_S) imaging (NCSI) technique [25] is used to simultaneously reveal the positions of both cations and anions, guarantying picometer precision measurements of the off-center displacements for evaluating the unit-cell dipole moments [24] (see also Refs. [26–30] therein). Combining the experimental measurements with first-principle calculations, the relation between the greatly enhanced polarization and the strain state is explored.

*zplmse@ustb.edu.cn
†c.jia@mail.xjtu.edu.cn

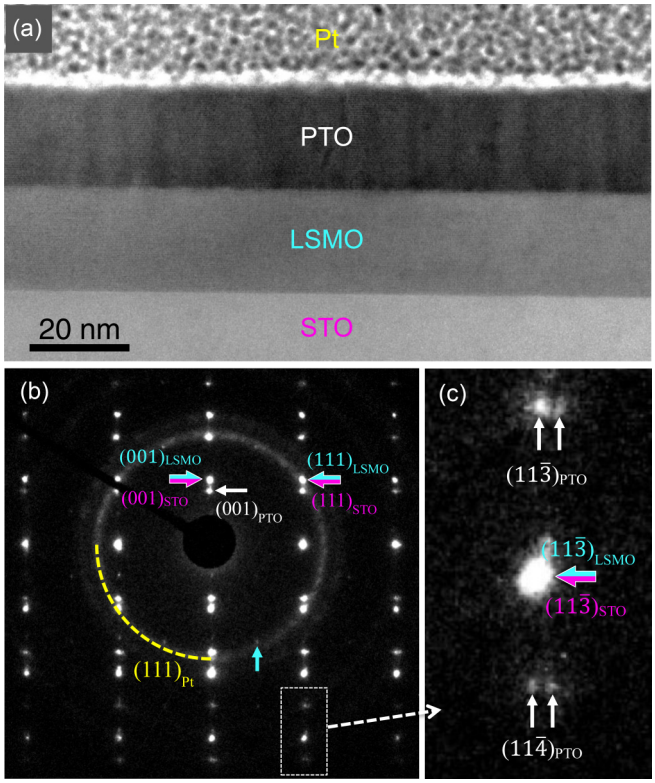

FIG. 1. (a) Low-magnification overview of the PTO/LSMO thin film on the STO substrate. (b) SAED pattern recorded along the $[1\bar{1}0]$ zone axis of the STO. Some of the diffraction spots are indexed, cyan: LSMO, magenta: STO, and white: PTO. The spot marked by the vertical arrow originates uniquely from LSMO as a result of rhombohedral or orthorhombic distortion. (c) Enlargement of part of the diffraction pattern, showing the splitting of high index reflections of the PTO film.

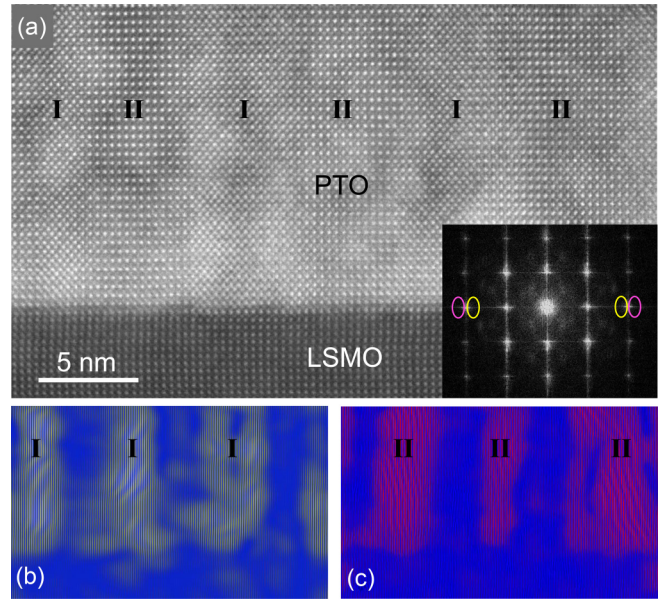

FIG. 2. (a) High-resolution HAADF image of the PTO film layer, in cross-section view along the [100] direction. Two types of columnar grains, type I and type II, are clearly seen with intergrowth on the nanometer scale. The inset shows the FFT diagram of the image. Circles indicate the numerical apertures used for the inverse FFT to obtain the images shown in (b) and (c), which are analogous to the dark-field images.

II. RESULTS

Figure 1(a) shows a cross-sectional overview of a PTO/LSMO ($La_{0.3}Sr_{0.7}MnO_3$) film on the STO substrate. The interfaces of PTO/LSMO/STO are sharp and clearly revealed. In the PTO film the visible vertical columnar contrast represents the feature of microstructures. Figure 1(b) shows a selected-area electron diffraction (SAED) pattern, which was recorded with the selected area aperture covering the PTO/LSMO film, the Pt top protection layer, and part of the substrate along the $[1\bar{1}0]$ zone axis of STO. The reflection spots were identified and some of them are indexed in the pattern. In order to simplify the following discussion, we disregard the lattice (rhombohedral or orthorhombic) distortion of the LSMO structure and describe it as a pseudocubic perovskite structure. In the diffraction pattern the fundamental spots of the LSMO film layer (cyan arrows) overlap with those of the STO substrate (magenta arrows), suggesting that the lattice parameter of the LSMO film is the same as that of the STO substrate. However, the spots (indicated by white arrows) of the PTO film are well separated from those of LSMO/STO, indicating a large difference in the out-of-plane lattice parameters c. In addition, we note that the high index diffraction spots of the PTO film show slight separation, as shown in Fig. 1(c), indicating the presence of structural variation or phases separation. Taking the diffraction ring of the Pt top layer as the calibration standard, the lattice parameters of the film system were measured and calculated. The c-lattice parameter for the PTO film is about 0.469 nm, which is much larger than the bulk value (0.4154 nm). According to the separation between the diffraction spots shown in Fig. 1(c), the in-plane lattice parameter a of the PTO film is found with two values, $a_1 = 0.395$ nm and $a_2 = 0.384$ nm.

Figure 2(a) shows a high-resolution high-angle annular dark-field (HAADF) STEM image of the PTO film layer and a part of the LSMO film layer, recorded along the [100] direction of the PTO. In the PTO film layer, two types of column grains can be clearly seen, denoted as type I and type II. The difference between the two types of column grains lies in the contrast from the B-site (Ti) atomic columns showing much lower intensities in columns II than those in columns I, as shown by the intensity profile in Fig. S1 [24]. The interfaces between the two types of columnar grains are lattice coherent, indicating same out-of-plane lattice spacing. Considering the separation between high index diffraction spots observed in Fig. 1(c), further investigation of the microstructure was performed with fast Fourier transform (FFT) of the image in Fig. 2(a). The inset to Fig. 2(a) shows the resulting FFT diagram, which is analogous to the diffraction pattern. On the diagram two types of numerical apertures (yellow and pink circles) are used for selecting the reflections corresponding to split of high index diffraction spots observed in Fig. 1(c). The two types of selected reflections were then used, respectively, to perform inverse FFTs, resulting in two images analogous to two dark-field images as shown in Figs. 2(b) and 2(c). The yellow areas in Fig. 2(b) are

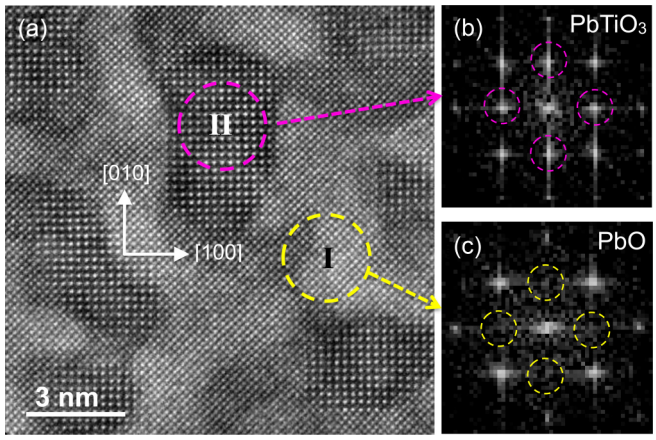

FIG. 3. (a) High-resolution HAADF image of the PTO film layer, in a plan view along the [001] direction. The type II columnar grains are embedded in the type I matrix. (b) FFT diagram of the type II columnar grain in image, leading to the identification of the PTO structure. (c) FFT diagram of the type I matrix in image, leading to identification of the PbO-type structure.

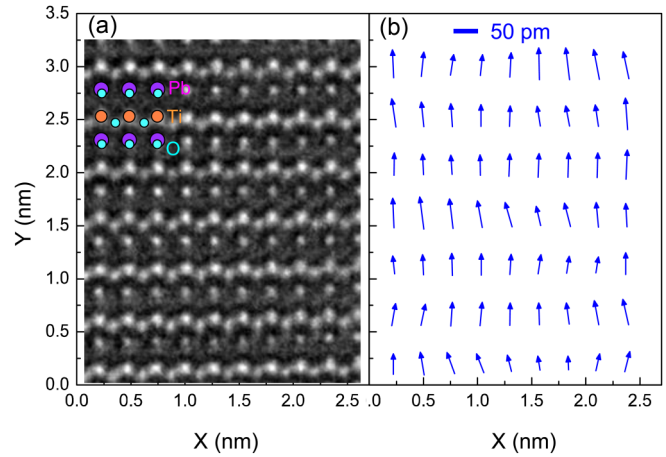

FIG. 4. (a) High-resolution NCSI image of a PTO grain, in a cross-sectional view along the $[1\bar{1}0]$ direction. In the image all types of atomic columns are well revealed, as denoted by the overlaid projected structure model (cyan: O, orange: Ti, purple: Pb). (b) Map of the displacement vectors of Ti columns with respect to the middle point of the line connecting two neighboring O atoms, which also represent the unit-cell dipole moments. The arrowheads point direction of the displacements and the length of each arrow represents the magnitude of the displacement.

formed from the reflections in the aperture of yellow circles, corresponding to columnar grains I, which have the lattice parameter $a_1 = 0.395$ nm. Similarly, the pink areas in Fig. 2(c) formed from the reflections in the pink aperture correspond to columnar grains II, which have the lattice parameter $a_2 = 0.384$ nm.

Figure 3(a) shows a plan-view HAADF image, revealing the presence of two types of structures, corresponding to the observed columnar grains in the cross-sectional sample in Fig. 2(a). From the plan-view image, the type II columnar grains are indeed surrounded by (or embedded in) the type I structure, which is imaged as columnar grains when it is cut to the cross section [Fig. 2(a)]. FFT was performed for the two structures on the plan-view image and the results are shown in Figs. 3(b) and 3(c), respectively. The evident difference in the FFT diagrams is marked by circles. Specifically, the reflections denoted by the pink circles from structure II disappear in the diagram from structure I, as indicated by the yellow circles. According to the image contrast and Fourier transforms, we identify the two phases as PTO structural phase (structure II) and PbO-type structural phase (structure I).

Chemical composition measurement using energy-dispersion x-ray analysis showed that the PbO-type phase also includes evidently Ti (Fig. S2) [24]. According to the cross-sectional and plan-view images, the lateral dimension of the PTO columnar grains is in the range of 3–5 nm. From investigations of the plan-view samples the volume fraction of the PTO phase is estimated to be about 30%. Based on the lattice parameters obtained from the diffraction analysis and those reported for the bulk materials, both lattices of the two compounds in the film are under strains. In particular, the PTO subjects to a very large tensile strain (about 13%) along the ***c***-axis direction, leading to a very strong lattice tetragonality of $c/a = 1.22$ in comparison to the value of $c/a = 1.06$ for bulk material.

To consider the coupling between the strain and the spontaneous polarization P_S in the PTO ferroelectric film, we quantified the off-center displacements of atoms, which lead to the formation of unit-cell dipoles and thus the macroscopic polarization. For this quantification, we used the NCSI technique to record atomic-resolution images, which reveal the positions of both cation and anion columns. Figure 4(a) shows a high-resolution image of a PTO grain, recorded under the NCSI condition along the $[1\bar{1}0]$ direction. Under the optimum imaging condition, the image of atomic columns appears bright under dark background, as shown by the projected structure model overlaid on the image (cyan: O; orange: Ti; purple: Pb). Comparison of the experimental image to the simulated image was carried out for evaluating the effects of the residual lens aberrations and unavoidable crystal tilt, as show in Figs. S3–S5 [24] (see also Refs. [26–30] therein). The simulated image, which shows the best match to the experimental one, is considered to represent the experimental image. Accordingly, the used parameters for the image calculation represent the imaging conditions used in the experiment, which lead to the conclusion that local image intensity maxima correctly represent the atomic positions. Therefore, based on the determined positions of these intensity maxima the off-center displacements of the Ti-atom columns were calculated with respect to the O-atom columns, which are displayed as a vector map in Fig. 4(b), where the arrows denote the displacement direction and the lengths of each arrow represent the magnitude of the displacements. The scale bar indicates a measure of the displacement magnitude and the corresponding polarization (or dipole moment) calculated according to the empirical relation $P_S = \kappa \cdot \Delta_{\mathrm{Ti-O}}$ [31], where $\Delta_{\mathrm{Ti-O}}$ is the Ti-atom off-center displacements with respect to O atoms and κ is a constant. On average, the measured displacement $\Delta_{\mathrm{Ti-O}}$ is about 0.052 nm. Since the dipole

direction is defined as starting from the negative charge center to the positive charge center, the polarization in the image area points upward. We have also observed the downward polarization in other columnar grains.

First-principle calculations were performed for the theoretical investigation of the relation between c/a, the off-center displacements, and the polarization [24] (see also Ref. [32] therein). The results after relaxation and optimization of the structure model show that the Ti atoms have an off-center displacement of 0.0516 nm with respect to the neighboring O atoms and $P_S = 122\,\mu C/cm^2$. The calculated Ti off-center displacement agrees well with the experimental data (see Table S1) [24]. The calculated polarization P_S will be compared to the results estimated using the empirical relation in the Discussion.

III. DISCUSSION

Our chemical composition investigation confirms the high-level solution of Ti element in the PbO-type structure. Since we did not detect any other Ti-rich phase in the film, the target stoichiometry of $PbTiO_3$ also implies the high-level solution of Ti in the PbO-type structured phase. Indeed, a PbO-TiO_2 solution was reported and the solubility of Ti can be as high as 80 at. % [33]. The PbO-TiO_2 solution with stoichiometry of $PbTi_{0.8}O_{2.6}$ was reported to have a similar tetragonal structure to PbO with lattice parameters of $a = 0.3911$ nm and $c = 0.4831$ nm. From our experimental results, the observed PbO-type structured phase in the present film is very close to that reported solution phase. Therefore, in the following discussion of strain, we take the lattice parameter of the $PbTi_{0.8}O_{2.6}$ phase as reference for the PbO-type structured phase in the present film. Unfortunately, in the reported research [33] no atomic structure was given. Therefore, the details about the atomic structure of the $PbTi_{0.8}O_{2.6}$ phase still need to be clarified.

Considering the lattice mismatches of bulk PTO, $PbTi_{0.8}O_{2.6}$, and STO, the strain level of the PTO columnar grains is much higher than that of the PbO-type structural matrix. This is well understandable considering that the columnar grains are embedded in the matrix, which forms a continuous film and produce a strong constraining force to the individually isolated PTO columnar grains. Meanwhile, the PTO columnar grains also react to the constraining force and thus exert a lattice strain on the matrix of the PbO-type structural phase. Reactions to the strain along the $\boldsymbol{c}$ axis and to the in-plane strain are also detected (Fig. S6) [24], which is represented by the splitting of the high index reflections in the electron diffraction pattern.

In coupling to the high strain of the PTO lattice and the strong tetragonality of the unit cell, the enhanced off-center displacements of atoms have been measured on the basis of quantitative determination of the cation and anion positions. Based on the empirical equation $P_S = \kappa \cdot \Delta_{Ti-O}$ [31] and the experimentally measured off-center displacements Δ_{Ti-O}, the polarization P_S of the PTO columnar grains has been estimated. We note that the value of κ was reported to be in the range from 2500 $(\mu C/cm^2)/nm$ to 2900 $(\mu C/cm^2)/nm$ for ferroelectric oxides [13,31,34,35]. Based on the range of the κ values the estimated P_S is between 130 and 150 $\mu C/cm^2$ for the present nanocolumnar grain, which is more than 60% higher than the value of bulk PTO (about 80 $\mu C/cm^2$). The coupling between strain and polarization has been widely investigated [1–3,13,22,36,37]. In particular, the continuous change of polarization with the tetragonality was experimentally characterized with respect to the off-center displacements of ions in the lead zirconate titanate thin film [36], the tetragonality of which is however in the range of tetragonality below 1.06. We note that there is still some discrepancy between the theoretically calculated polarization (122 $\mu C/cm^2$) and the calculated value using the empirical relation (130–150 $\mu C/cm^2$). The discrepancy may be partially understood as the results of the uncertainty in the experimental measurement of the atom displacements, which is about 0.005 nm leading to an uncertainty of 15 $\mu C/cm^2$ level [24,31]. In addition, our first-principle calculations showed that the Born effective charges for the highly strained film are about 10% smaller than that for the low-strained film or bulk samples. This reminds that the κ values in the empirical relations may be overestimated by approximately 10% for the highly strained film. Taking this factor into account, the polarization values calculated using the empirical relation can be considered to be smaller by 10%, leading to a polarization value in the range of 117–135 $\mu C/cm^2$, which fit well to the theoretically calculated value.

We note that the wide application of HAADF imaging to determine or estimate the polarization under high-strain states relies on the measured displacement of Ti (Δ_{Ti}) from its centrosymmetric position (or the center of the surrounding Pb atoms located on the corners of perovskite lattice as reference positions) following the equation: $P_{S[film]} = P_{S[bulk]}$ $\Delta_{Ti[film]}/\Delta_{Ti[bulk]} = \kappa \cdot \Delta_{Ti-O[bulk]}\Delta_{Ti[film]}/\Delta_{Ti[bulk]}$ [22,37], where $\Delta_{Ti-O[bulk]}/\Delta_{Ti[bulk]} \approx 2$ for PTO [34]. By doing so, one has to assume a linear relation of Δ_{Ti-O} with respect to Δ_{Ti}. However, it should be noted that the position of the peaks for the Ti columns is highly dependent on the thickness in the [100] HAADF image, which introduces additional artificial shift. The underlying reason for the artificial shift of the thickness dependence is largely affected by its neighboring O atoms. Therefore, for the estimation of the polarization one has to remove the artificial shift from the simple measurement on a [100] HAADF image by comparison to image simulations. Therefore, the present research, on the atomic scale, provides details for the relation between tetragonality and the off-center displacements of atoms including oxygen as well as polarization under such a high strain. It is important to note that the experimental results have been supported by first-principle calculations based on both GPAW [38] and ABINIT [39].

We note that the strained PTO in the PbO-type matrix did not develop a similar polarization as previously reported ($P_S = 236\,\mu C/cm^2$) [22] where only the off-center displacements of the so-called Ti atoms (actually influenced by the neighboring O as mentioned above) were given, while the measured c- and a-lattice parameters (and thus the tetragonality) for both films are almost the same. Considering the important role of oxygen anions in determining the polarization, without positional details of the oxygen atoms in the unit

cell, it is hard to understand quantitatively the behavior of the polarization. Therefore, the mechanism for such a high value of polarization [22] remains unclear.

IV. CONCLUSION

In summary, the structural origin for the highly enhanced polarization of the PTO columnar grains is characterized by means of atomic-resolution (S)TEM and first-principles calculations. The enhanced polarization lies in the strong off-center displacements of the atoms, which are directly revealed by imaging all the atoms including oxygen and confirmed by first-principle calculations. The measured displacement fits excellently with that obtained by calculations. The enhanced off-center displacements are coupled with the huge strain in the PTO columnar grains, which is induced by the surrounding lattice of the PbO-type structure matrix.

ACKNOWLEDGMENTS

The authors thank Shaodong Cheng for the help in preparation of the plan-view sample. L.L. acknowledges the support of National Natural Science Foundation of China, Grant No. 51901172. F.Z. and D.W.W. acknowledge the support of National Natural Science Foundation of China, Grant No. 11974268. Y.J. and Z.P.L. acknowledge the support of the Fundamental Research Funds for the Central Universities (Grant No. FRF-MP-20-27).

[1] A. R. Damodaran, J. C. Agar, S. Pandya, Z. H. Chen, L. Dedon, R. J. Xu, B. Apgar, S. Saremi, and L. W. Martin, New modalities of strain-control of ferroelectric thin films, J. Phys.: Condens. Matter **28**, 263001 (2016).

[2] X. W. Jin, L. Lu, S. B. Mi, M. Liu, and C. L. Jia, Phase stability and B-site ordering in La_2NiMnO_6 thin films, Appl. Phys. Lett. **109**, 031904 (2016).

[3] L. W. Martin and A. M. Rappe, Thin-film ferroelectric materials and their applications, Nat. Rev. Mater. **2**, 16087 (2017).

[4] K. J. Choi, M. Biegalski, Y. L. Li, A. Sharan, J. Schubert, R. Uecker, P. Reiche, Y. B. Chen, X. Q. Pan, V. Gopalan, L.-Q. Chen, D. G. Schlom, and C. B. Eom, Enhancement of ferroelectricity in strained $BaTiO_3$ thin films, Science **306**, 1005 (2004).

[5] J. H. Haeni, P. Irvin, W. Chang, R. Uecker, P. Reiche, Y. L. Li, S. Choudhury, W. Tian, M. E. Hawley, B. Craigo, A. K. Tagantsev, X. Q. Pan, S. K. Streiffer, L. Q. Chen, S. W. Kirchoefer, J. Levy, and D. G. Schlom, Room-temperature ferroelectricity in strained $SrTiO_3$, Nature (London) **430**, 758 (2004).

[6] J. L. MacManus-Driscoll, P. Zerrer, H. Y. Wang, H. Yang, J. Yoon, A. Fouchet, R. Yu, M. G. Blamire, and Q. X. Jia, Strain control and spontaneous phase ordering in vertical nanocomposite heteroepitaxial thin films, Nat. Mater. **7**, 314 (2008).

[7] S. A. Harrington, J. Zhai, S. Denev, V. Gopalan, H. Wang, Z. Bi, S. A. T. Redfern, S. H. Baek, C. W. Bark, C. B. Eom, Q. Jia, M. E. Vickers, and L J. MacManus-Driscoll, Thick lead-free ferroelectric films with high Curie temperatures through nanocomposite-induced strain, Nat. Nanotechnol. **6**, 491 (2011).

[8] A. P. Chen, Z. X. Bi, Q. X. Jia, J. L. MacManus-Driscoll, and H. Y. Wang, Microstructure, vertical strain control and tunable functionalities in self-assembled, vertically aligned nanocomposite thin films, Acta Mater. **61**, 2783 (2013).

[9] X. Sun, Q. Li, J. J. Huang, M. Fan, B. X. Rutherford, R. L. Paldi, J. Jian, X. H. Zhang, and H. Y. Wang, Strain-driven nanodumbbell structure and enhanced physical properties in hybrid vertically aligned nanocomposite thin films, Appl. Mater. Today **16**, 204 (2019).

[10] E. Enriquez, Q. Li, P. Bowlan, P. Lu, B. Zhang, L. Li, H. Wang, A. J. Taylor, D. Yarotski, R. P. Prasankumar, S. V. Kalinin, Q. Jia, and A. Chen, Induced ferroelectric phases in $SrTiO_3$ by a nanocomposite approach, Nanoscale **12**, 18193 (2020).

[11] R. E. Cohen, Origin of ferroelectricity in perovskite oxides, Nature (London) **358**, 136 (1992).

[12] C. Lichtensteiger, J. M. Triscone, J. Junquera, and P. Ghosez, Ferroelectricity and Tetragonality in Ultrathin $PbTiO_3$ Films, Phys. Rev. Lett. **94**, 047603 (2005).

[13] C. L. Jia, V. Nagarajan, J. Q. He, L. Houben, T. Zhao, R. Ramesh, K. Urban, and R. Waser, Unit-cell scale mapping of ferroelectricity and tetragonality in epitaxial ultrathin ferroelectric films, Nat. Mater. **6**, 64 (2007).

[14] L. Jin, C. L. Jia, and I. Vrejoiu, Engineering 180 degrees ferroelectric domains in epitaxial $PbTiO_3$ thin films by varying the thickness of the underlying $(La,Sr)MnO_3$ layer, Appl. Phys. Lett. **105**, 132903 (2014).

[15] A. R. Damodaran, S. Pandya, J. C. Agar, Y. Cao, R. K. Vasudevan, R. Xu, S. Saremi, Q. Li, J. Kim, M. R. McCarter, L. R. Dedon, T. Angsten, N. Balke, S. Jesse, M. Asta, S. V. Kalinin, and L. W. Martin, Three-state ferroelastic switching and large electromechanical responses in $PbTiO_3$ thin films, Adv. Mater. **29**, 1702069 (2017).

[16] A. K. Yadav, K. X. Nguyen, Z. Hong, P. García-Fernández, P. Aguado-Puente, C. T. Nelson, S. Das, B. Prasad, D. Kwon, S. Cheema, A. I. Khan, C. Hu, J. Íñiguez, J. Junquera, L. Q. Chen, D. A. Muller, R. Ramesh, and S. Salahuddin, Spatially resolved steady-state negative capacitance, Nature (London) **565**, 468 (2019).

[17] C. L. Jia, K. W. Urban, M. Alexe, D. Hesse, and I. Vrejoiu, Direct observation of continuous electric dipole rotation in flux-closure domains in ferroelectric $Pb(Zr, Ti)O_3$, Science **331**, 1420 (2011).

[18] Y. L. Tang, Y. L. Zhu, X. L. Ma, A. Y. Borisevich, A. N. Morozovska, E. A. Eliseev, W. Y. Wang, Y. J. Wang, Y. B. Xu, Z. D. Zhang, and S. J. Pennycook, Observation of a periodic array of flux-closure quadrants in strained ferroelectric $PbTiO_3$ films, Science **348**, 547 (2015).

[19] A. K. Yadav, C. T. Nelson, S. L. Hsu, Z. Hong, J. D. Clarkson, C. M. Schlepütz, A. R. Damodaran, P. Shafer, E. Arenholz, L. R. Dedon, D. Chen, A. Vishwanath, A. M. Minor, L. Q. Chen, J. F. Scott, L. W. Martin, and R. Ramesh, Observation of polar vortices in oxide superlattices, Nature (London) **530**, 198 (2016).

[20] S. Das, Y. L. Tang, Z. Hong, M. A. P. Gonçalves, M. R. McCarter, C. Klewe, K. X. Nguyen, F. Gómez-Ortiz, P. Shafer,

E. Arenholz, V. A. Stoica, S. L. Hsu, B. Wang, C. Ophus, J. F. Liu, C. T. Nelson, S. Saremi, B. Prasad, A. B. Mei, D. G. Schlom, J. Íñiguez, P. García-Fernández, D. A. Muller, L. Q. Chen, J. Junquera, L. W. Martin, and R. Ramesh, Observation of room-temperature polar skyrmions, Nature (London) **568**, 368 (2019).

[21] L. Lu, Y. Nahas, M. Liu, H. Du, Z. Jiang, S. Ren, D. Wang, L. Jin, S. Prokhorenko, C. L. Jia, and L. Bellaiche, Topological Defects with Distinct Dipole Configurations in $PbTiO_3/SrTiO_3$ Multilayer Films, Phys. Rev. Lett. **120**, 177601 (2018).

[22] L. Zhang, J. Chen, L. Fan, O. Diéguez, J. Cao, Z. Pan, Y. Wang, J. Wang, M. Kim, S. Deng, J. Wang, H. Wang, J. Deng, R. Yu, J. F. Scott, and X. Xing, Giant polarization in super-tetragonal thin films through interphase strain, Science **361**, 494 (2018).

[23] Z. Zhang, Y. Z. Dai, Z. Li, L. Lu, X. Zhang, K. Fu, X. Xu, W. Tian, C. L. Jia, and Y. Jiang, Growth modulation of super-tetragonal $PbTiO_3$ thin films with self-assembled nanocolumn structures, Adv. Electron. Mater. **7**, 2100547 (2021).

[24] See Supplemental Material at http://link.aps.org/supplemental/10.1103/PhysRevB.104.184111 for fabrication of multilayer films, electron microscopy and analysis, first-principle calculations, Figs. S1–S6, and Table S1.

[25] C. L. Jia, M. Lentzen, and K. Urban, Atomic-resolution imaging of oxygen in perovskite ceramics, Science **299**, 870 (2003).

[26] L. Houben, iMtools electron microscope image processing software, Forschungszentrum Jülich http://www.er-c.org/methods/software.htm (June 2014).

[27] C. L. Jia, S. B. Mi, K. Urban, I. Vrejoiu, M. Alexe, and D. Hesse, Atomic-scale study of electric dipoles near charged and uncharged domain walls in ferroelectric films, Nat. Mater. **7**, 57 (2008).

[28] C. L. Jia, J. Barthel, F. Gunkel, R. Dittmann, S. Hoffmann-Eifert, L. Houben, M. Lentzen, and A. Thust, Atomic-scale measurement of structure and chemistry of a single-unit-cell layer of LaAlO3 embedded in $SrTiO_3$, Microsc. Microanal. **19**, 310 (2013).

[29] R. Kilaas, *Proceedings of the 45th Annual Meeting of the Electron Microscopy Society of America, Baltimore, MD*, edited by G. W. Bailey (San Francisco Press, San Francisco, 1987), pp. 66–67.

[30] C. L. Jia, L. Houben, A. Thust, and J. Barthel, On the benefit of the negative-spherical-aberration imaging technique for quantitative HRTEM, Ultramicroscopy **110**, 500 (2010).

[31] S. C. Abrahams, S. K. Kurtz, and P. B. Jamieson, Atomic displacement relationship to curie temperature and spontaneous polarization in displacive ferroelectrics, Phys. Rev. **172**, 551 (1968).

[32] J. P. Perdew, K. Burke, and M. Ernzerhof, Generalized Gradient Approximation Made Simple, Phys. Rev. Lett. **77**, 3865 (1996).

[33] H. M. Cheng, J. M. Ma, and Z. G. Zhao, Hydrothermal synthesis of PbO-TiO2 solid solution, Chem. Mater. **6**, 1033 (1994).

[34] A. M. Glazer and S. A. Mabud, Powder profile refinement of lead zirconate titanate at several temperatures. II. Pure $PbTiO_3$, Acta Crystallogr. B **34**, 1065 (1978).

[35] C. T. Nelson, B. Winchester, Y. Zhang, S. J. Kim, A. Melville, C. Adamo, C. M. Folkman, S. H. Baek, C. B. Eom, D. G. Schlom, L. Q. Chen, and X. Pan, Spontaneous vortex nanodomain arrays at ferroelectric heterointerfaces, Nano Lett. **11**, 828 (2011).

[36] C. L. Jia, S. B. Mi, K. Urban, I. Vrejoiu, M. Alexe, and D. Hesse, Effect of a Single Dislocation in a Heterostructure Layer on the Local Polarization of a Ferroelectric Layer, Phys. Rev. Lett. **102**, 117601 (2009).

[37] J. Wang, B. Wylie-van Eerd, T. Sluka, C. Sandu, M. Cantoni, X. K. Wei, A. Kvasov, L. J. McGilly, P. Gemeiner, B. Dkhil, A. Tagantsev, J. Trodahl, and N. Setter, Negative-pressure-induced enhancement in a freestanding ferroelectric, Nat. Mater. **14**, 985 (2015).

[38] J. Enkovaara, C. Rostgaard, J. J. Mortensen, J. Chen, M. Dułak, L. Ferrighi, J. Gavnholt, C. Glinsvad, V. Haikola, H. A. Hansen, H. H. Kristoffersen, M. Kuisma, A. H. Larsen, L. Lehtovaara, M. Ljungberg, O. Lopez-Acevedo, P. G. Moses, J. Ojanen, T. Olsen, V. Petzold, N. A. Romero, J. Stausholm-Møller, M. Strange, G. A. Tritsaris, M. Vanin, M. Walter, B. Hammer, H. Häkkinen, G. K. H. Madsen, R. M. Nieminen, J. K. Nørskov, M. Puska, T. T. Rantala, J. Schiøtz, K. S. Thygesen, and K. W. Jacobsen, Electronic structure calculations with GPAW: A real-space implementation of the projector augmented-wave method, J. Phys.: Condens. Matter **22**, 253202 (2010).

[39] X. Gonze, B. Amadon, G. Antonius, F. Arnardi, L. Baguet, J.-M. Beuken, J. Bieder, F. Bottin, J. Bouchet, E. Bousquet, N. Brouwer, F. Bruneval, G. Brunin, T. Cavignac, J.-B. Charraud, W. Chen, M. Côté, S. Cottenier, J. Denier, G. Geneste, P. Ghosez, M. Giantomassi, Y. Gillet, O. Gingras, D. R. Hamann, G. Hautier, X. He, N. Helbig, N. Holzwarth, Y. Jia, F. Jollet, W. Lafargue-Dit-Hauret, K. Lejaeghere, M. A. L. Marques, A. Martin, C. Martins, H. P. C. Miranda, F. Naccarato, K. Persson, G. Petretto, V. Planes, Y. Pouillon, S. Prokhorenko, F. Ricci, G. M. Rignanese, A. H. Romero, M. M. Schmitt, M. Torrent, M. J. van Setten, B. Van Troeye, M. J. Verstraete, G. Zérah, and J. W. Zwanziger, The Abinit project: Impact, environment and recent developments, Comput. Phys. Commun. **248**, 107042 (2020).